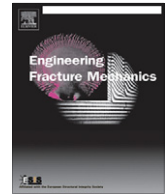




ELSEVIER

Contents lists available at SciVerse ScienceDirect

Engineering Fracture Mechanics

journal homepage: www.elsevier.com/locate/engfracmech

Hardening cohesive/overlapping zone model for metallic materials: The size-scale independent constitutive law

Alberto Carpinteri*, Baoming Gong, Mauro Corrado

Department of Structural Engineering and Geotechnics, Politecnico di Torino, Corso Duca degli Abruzzi 24, 10129 Torino, Italy

ARTICLE INFO

Article history:

Received 1 April 2011

Received in revised form 9 November 2011

Accepted 24 November 2011

Keywords:

Metals

Ductile fracture

Cohesive zone model

Overlapping zone model

Limit analysis

Fractals

ABSTRACT

A new hardening cohesive/overlapping zone model for metallic materials based on Nonlinear Fracture Mechanics concepts is proposed to capture the ductile fracture phenomena. The fracture and compression behaviors of an initially cracked specimen are described by the cohesive zone model and the overlapping zone model, respectively. Both approaches assume a stress vs. displacement (fictitious opening or interpenetration) constitutive law to describe the hardening and softening behaviors in the process zones in tension and compression. As a result, the cohesive/overlapping zones are considered to be representative of the regions where the plastic dissipation in the bulk and the crack formation and propagation take place. The proposed model is applied to study the size effects in three-point-bending and compact tension tests. Furthermore, the asymptotical post-peak performances of load vs. deflection curves are determined through the plastic limit analysis using the proposed model. In this context, the fractal approach is applied to obtain scale-independent hardening cohesive/overlapping laws. Finally, experimental confirmations to the numerical simulations and to the limit analysis are discussed.

© 2011 Elsevier Ltd. All rights reserved.

1. Introduction

In the framework of Linear Elastic Fracture Mechanics (LEFMs), the symmetrical stress field around the crack tip is usually characterized by a single fracture toughness parameter, such as the stress-intensity factor, K_I , or the energy release rate, \mathcal{G}_I . Their critical values are frequently used as criteria for crack initiation. However, these concepts are based on linear elasticity and they are invalid when plastic yielding takes place at the front of the crack tip. The path independent J -integral was proposed as crack initiation criterion for nonlinear elastic materials without unloading [1]. However, it is now generally accepted that the J -integral resistance curves may be significantly influenced by loading conditions and specimen sizes. Moreover, in most practical conditions, it is not able to characterize the fracture “driving force” in the presence of finite inelastic energy dissipation and unloading processes. Alternatively, the crack growth resistance curve in terms of K , \mathcal{G} or J has been obtained vs. crack extension Δa , namely, $\Gamma = \Gamma(\Delta a)$ [2]. A crack starts to propagate at $\Gamma = \Gamma_0$, then it grows in a stable manner with increasing Γ , and finally becomes unstable when $\Gamma = \Gamma_{ss}$ (see Fig. 1). Typically, Γ_{ss} is much larger than Γ_0 and depends on the additional irreversible processes by remote and local plastic energy dissipation in the bulk. Unfortunately, the resistance curve cannot be considered as a material property due to its significant dependence on specimen size, initial crack length and/or loading configuration. Therefore, it is reasonable in ductile fracture to postulate that the total energy release rate comprises the energy dissipation rate referred to the plasticization of the material surrounding the process zone and the separation energy rate required to create new fracture surfaces, according to the concept of the energy dissi-

* Corresponding author. Tel.: +39 011 0904850; fax: +39 011 0904899.

E-mail address: alberto.carpinteri@polito.it (A. Carpinteri).

Notation

a_0	initial crack length
B	thickness of specimen
$\{F\}$	vector of nodal forces
F_y	yielding force
\mathcal{G}_F	fracture energy
\mathcal{G}_C	crushing energy
h	extension of cohesive zone or overlapping zone
L	span of the specimen
γ	hardening exponent
$[K_w]$	matrix of the coefficients of influence for the nodal displacements
$[K_P]$	vector of the coefficients of influence for the applied force
P	applied force
s_E	energy brittleness number
W	depth of the beam or width of the CT specimen
$\{w\}$	vector of nodal displacements (crack opening/overlapping relative displacements)
w_{cr}	critical crack opening/overlapping displacement
w_r	opening/overlapping displacement at the peak cohesive stress
k	w_r/w_{cr}
δ	deflection or load-line displacement
ε_y	yielding strain
ξ_0	initial crack ratio
λ	$L/W =$ specimen slenderness
σ	stress
σ_y	yielding stress
σ_u	ultimate stress

pation rate introduced by Turner and Kolednik [3] and Sumpter [4]. This is a straight generalization of the Griffith's elastic energy release rate to fracture processes with bulk plastic deformation.

As mentioned above, LEFM has been proven to be useful only if a crack-like notch or flaw exists in the body when the size of the process zone due to plasticity or microcracking can be negligible with respect to the dimensions of the structural element. However, these conditions are not always fulfilled, both for ductile metals and quasi-brittle cementitious materials, for which the *Cohesive Zone Model* (CZM) proposed by Barenblatt [5,6] and Dugdale [7] was proven to be versatile. Subsequently, the Dugdale model was reconsidered by Bilby et al. [8], Willis [9], Rice [1], and utilized by Wnuk [10]. Hillerborg et al. [11] proposed the *Fictitious Crack Model* in order to study crack propagation in concrete. The model was further applied by Wecharatana and Shah [12], Bažant and Oh [13], and Ingraffea and Gerstle [14]. More recently, the former terminology of *cohesive crack model* has been repropoed by Carpinteri [15–18], and Carpinteri et al. [19–21] to solve the unstable snap-back behaviors. The model has been used with this name by a number of researchers [22–24]. Later on, in order to explain the size effects upon the parameters of the cohesive law, fractal geometry concepts were introduced to elaborate the influence of the microstructural disorder typical of quasi-brittle materials [25–28], giving rise to the so-called *fractal* (scale-invariant) *cohesive zone model* [29]. The model was applied to interpret the most extensive experimental tensile data from concrete specimens tested over a broad range of scales [30,31]. The review of those results is in [32]. Tvergaard and Hutchinson [33,34] discussed the applicability of the cohesive zone model in ductile fracture, where it was used only for the fracture process,

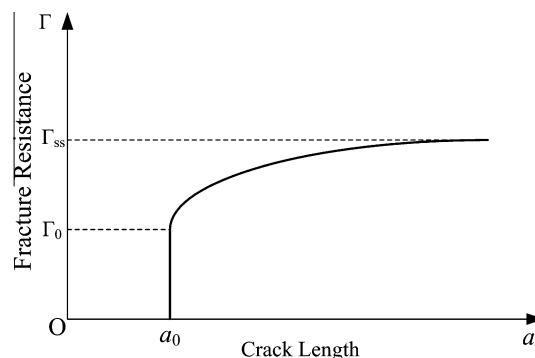


Fig. 1. Typical fracture resistance curve for ductile materials.

whereas the finite plastic deformations outside the fracture zone – as well as necking in initially uncracked tensile specimens – were taken into account through J_2 flow theory. Furthermore, Siegmund and Brocks [35] proposed a cohesive zone model in which the peak stress and the cohesive energy are functions of the stress triaxiality calculated by the Gurson model which, is widely used for ductile materials [36–38]. More precisely, they suggested that the energy dissipation rate consists of a global plastic dissipation rate in the volume and a local separation energy (or local work of separation). The triaxiality dependent cohesive zone model was used to investigate the effects of specimen size and initial crack extension on crack growth resistance behaviors in ductile fracture [39].

2. Constitutive models

2.1. Basic concepts of the cohesive zone model

The basic assumption of the cohesive zone model is the formation, as an extension of the real crack, of a fictitious crack, referred to as the process zone, where the material, albeit damaged, is still able to transfer stresses. The point separating the stress-free area, i.e., the real crack, from the process zone, is called real crack tip, whilst the point separating the process zone from the uncracked material is referred to as fictitious crack tip. The process zone represents the area in which energy dissipation takes place: it begins where the principal tensile stress reaches the material tensile strength, and propagates in the direction perpendicular to the direction of the principal tensile stress. In the process zone, the stresses transferred by the material are functions of the displacement discontinuity, according to a proper cohesive law, whilst in the uncracked zone the behavior of the material is linear-elastic or elasto-plastic. In the model described so far, shearing stresses in the process zone are disregarded. The area under the σ vs. w curve represents the fracture energy, G_f , usually considered as a material property. At the fictitious crack tip, the stress will be always equal to the tensile strength, and it is generally assumed that no stress singularities exist at the fictitious crack tip. Some cohesive zone models may share the common character that the cohesive traction at the fictitious tip is zero. However, from a physical point of view, the cohesive law describes the progressive fracture process induced by finite deformation or applied stress. It is thus reasonable that the initial value of the traction vs. separation law should be different from zero. Mathematically, the cohesive law with an initial zero traction does not guarantee the absence of stress singularity at the fictitious crack tip, as demonstrated by Jin and Sun [40].

2.2. Basic concepts of the overlapping zone model

In the field of quasi-brittle materials, the *overlapping zone model* has been recently proposed in [41,42]. In close analogy with the cohesive zone model, the localized compressive behavior of such materials is modelled by means of a compressive stress vs. fictitious interpenetration law, whereas a linear-elastic stress vs. strain relationship is assumed for the undamaged material. The material in the process zone is assumed to be able to transfer compressive stresses through the overlapping surfaces, which are functions of the fictitious overlapping relative displacement, w . The localized compressive zone is then represented by a fictitious overlapping, which is mathematically analogous to the fictitious crack in tension (see Fig. 2b). The overlapping zone develops when the maximum compressive stress achieves the compression strength, and, in general, it is assumed to propagate perpendicularly to it. Moreover, the area under the stress vs. displacement curve is defined as the crushing or overlapping energy, G_c (energy per unit area). It is worth noting that, contrarily to the cohesive zone model, that has a direct connection with the actual mechanical behavior of quasi-brittle materials subjected to tension, the overlapping zone model is just an idealization of an extremely complex failure mechanism that can vary from pure crushing to diagonal shearing or to splitting failures, depending on the specimen size-scale and/or slenderness.

2.3. Hardening cohesive/overlapping zone model

In the present study, a new simple model is proposed for metallic materials through the incorporation of cohesive and overlapping zone models. As regards the tensile behavior, differently to previous applications, where the use of the cohesive crack model was limited to the softening regime, in the proposed approach the localization is considered also in the hard-

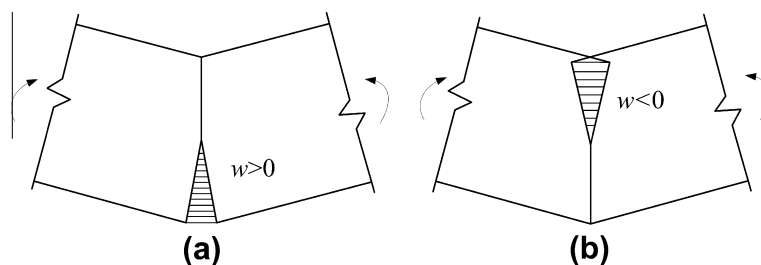


Fig. 2. Fracture with cohesive zone (a); compression with overlapping zone (b).

ening phase. This means that, the process zone of the cohesive zone model is representative of the region where the plastic dissipation in the bulk and the crack formation and propagation take place, i.e., the necking zone. The material outside the necking has a linear-elastic behavior. Accordingly, the mechanical behavior of a metallic specimen under uniaxial tension can be divided into the following stages:

- (a) The specimen is elastic without any damage or localized zone (see Fig. 3b). The constitutive law is that shown in Fig. 4a, and the specimen elongation is:

$$\delta = \varepsilon L = \sigma L/E, \quad \text{for } \sigma < \sigma_y. \tag{1}$$

- (b) After the elastic limit is overcome, the deformation starts to localize within a limited specimen portion, giving rise to the well-known phenomenon of necking (Fig. 3c). In case a perfectly plastic behavior is considered (constitutive law in Fig. 4b), the applied load remains constant whereas the localized displacement, w , increases up to the limit value w_r . The total elongation of the specimen is:

$$\delta = \sigma_y L/E + w, \quad \text{for } w \leq w_r. \tag{2}$$

The elastic contribution of the bulk material is constant.

- (c) As the necking deformation proceeds, microvoids enlargement and coalescence lead to the softening behavior, with $\sigma < \sigma_u$ and $w_r < w \leq w_{cr}$, as shown in Fig. 3d. The localized contribution still increases, whereas the elastic one decreases according to the loading decrement. When $w > w_{cr}$, the reacting stress vanishes, and the material in the necking zone is completely failed and unable to bear any loading, i.e. $\sigma = 0$ (see Fig. 3e).

As a result, the predicted overall behavior in tension is scale-dependent, as shown in Fig. 5. In particular, when $w_{cr} > (L\varepsilon_y + w_r)$, the softening process is stable if displacement-controlled, since the slope $d\sigma/d\delta$ of the softening branch is negative (see Fig. 5a). On the contrary, when $w_{cr} < (L\varepsilon_y + w_r)$, the slope $d\sigma/d\delta$ of the softening branch becomes positive (*snap-back*), as shown in Fig. 5b. In this case the loading process is stable only if it is controlled through a parameter that is a monotonic increasing function of time, such as, for instance, the circumferential contraction in the necking region. The condition of snap-back can be rearranged as follows:

$$\frac{w_{cr}(1-k)/2W}{\varepsilon_y(L/W)} < \frac{1}{2}, \tag{3}$$

where W is the specimen width, and $k = w_r/w_{cr}$. In the case of perfectly-plastic law, w_{cr} can be expressed by means of σ_y , G_F and k , and, therefore, Eq. (3) may be rewritten in the following form:

$$s_E \frac{1}{\varepsilon_y \lambda} \frac{1-k}{1+k} \leq \frac{1}{2}, \tag{4}$$

where

$$s_E = \frac{G_F}{\sigma_y W} \tag{5}$$

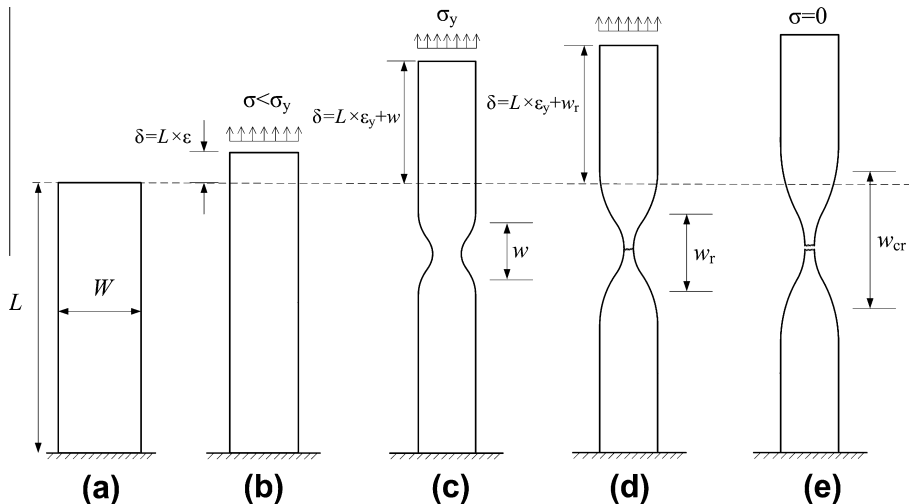


Fig. 3. Different stages of the deformation history: (a) original without load; (b) no damage; (c) yielding and necking; (d) microscale crack; (e) final failure.

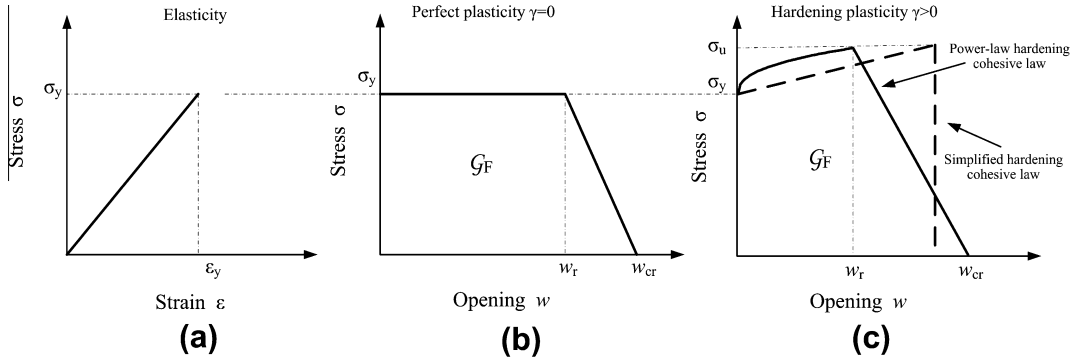


Fig. 4. Constitutive laws according to the cohesive/overlapping zone model: (a) linear-elastic stress vs. strain relationship for the undamaged material; (b) perfectly plastic stress vs. displacement law for the damaged and/or yielded material (followed by a softening tail) for perfect plasticity ($\gamma = 0$), and (c) hardening plasticity ($\gamma > 0$).

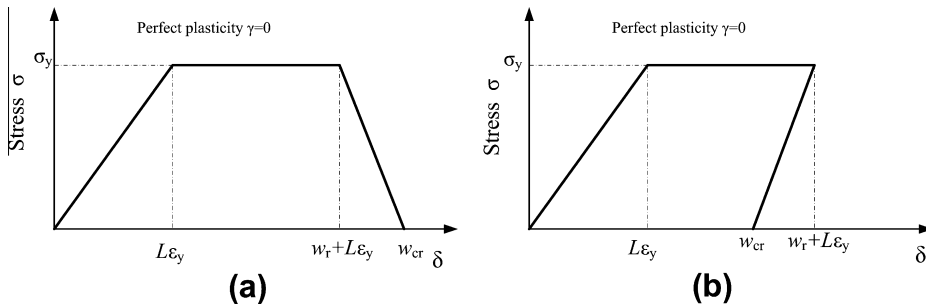


Fig. 5. Stress vs. displacement response for perfectly plastic material: (a) normal softening; (b) snap-back instability.

is the energy brittleness number, a function of the mechanical and geometrical parameters of the problem, (introduced by Carpinteri [15–18] for quasi-brittle materials), and $\lambda = L/W$ is the specimen slenderness.

It is worth noting that the application of Eq. (2) permits the hardening cohesive law and its parameters to be directly derived from the experimental load vs. elongation curves. In the present study, a symmetric behavior for tension and compression is considered on the basis of the failure mechanism occurring at the microscale. For crystalline solids under either tension or compression, in fact, deformation and failure are accomplished by means of dislocation motions, which involve the dislocation nucleation, slipping and annihilation, leading to very similar tensile and compressive stress–strain behaviors into the plastic region [43]. In compression, since necking does not occur, the plastic flow under uniaxial compression will be localized and developed into a slip band with an orientation of about 45° to the loading direction, similar to the localized tensile necking. These localizations of irreversible energy dissipation in terms of plasticity and fracture are not rigorously interpretable in continuum mechanics, although they have significant effects on ductility.

In the following, more complex cohesive/overlapping constitutive relations are considered, taking the hardening effect into account. The stress vs. displacement laws are such that the stresses undergo a power-law hardening as the displacements increase up to the ultimate stress σ_u (solid line in Fig. 4c):

$$\sigma = \sigma_y + (\sigma_u - \sigma_y)(w/w_r)^\gamma, \tag{6}$$

where $\gamma > 0$ is the hardening exponent, $\gamma = 0$ corresponding to perfect plasticity; σ_y is the yielding stress; w is the opening or overlapping relative displacement; w_r corresponds to the peak stress and determines the shape of the stress vs. separation law. Beyond the displacement w_r , the stresses may decrease in different ways and vanish in correspondence with the critical value for the opening or overlapping relative displacement, w_{cr} . A linear elastic stress vs. strain law is adopted for the undamaged material (Fig. 4a).

3. Numerical algorithm

Let us consider the three-point-bending (TPB) specimen shown in Fig. 6. On the basis of the constitutive laws previously introduced for metallic materials, the fracturing and the plastic phenomena taking place within the mid-span portion can be described by means of the numerical approach proposed by Carpinteri et al. [41] for reinforced concrete beams. Such an approach is based on a discrete form of the elastic equations governing the mechanical response of the two symmetric portions.

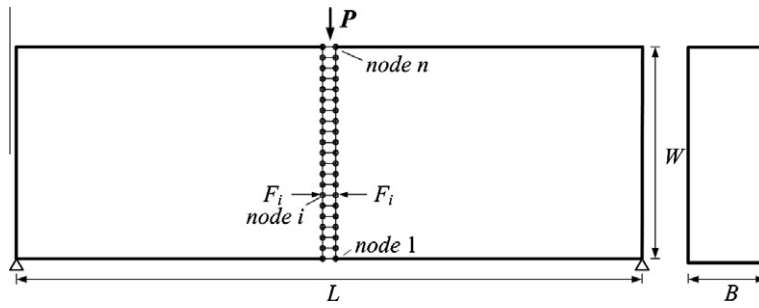


Fig. 6. Finite element nodes along the mid-span cross-section of the TPB specimen.

In this scheme, both fracturing and plastic compressive phenomena are assumed to be fully localized along the mid-span cross-section of the beam. The symmetry cross-section of the specimen can be subdivided into finite elements by n nodes. Consequently, cohesive and overlapping stresses are replaced by equivalent nodal forces by integrating the corresponding distributed tractions over the element side. Such nodal forces depend on the nodal opening or overlapping displacements according to the cohesive or overlapping laws shown in Fig. 4c. The nodal forces, F_i , acting along the mid-span cross-section can be computed as follows:

$$\{F\} = [K_w]\{w\} + \{K_p\}P, \tag{7}$$

where $\{F\}$ is the vector of nodal forces, $[K_w]$ is the matrix of the coefficients of influence for the nodal displacements, $\{w\}$ is the vector of nodal displacements, and $\{K_p\}$ is the vector of the coefficients of influence for the applied load P . All the coefficients of influence are computed *a priori* with a linear-elastic finite element analysis. In addition, $[K_w]$ and $\{K_p\}$ are independent of the specimen size, mesh and slenderness ratio being the same. When fracturing and compression yielding take place, the following equations can be considered (see Fig. 7):

$$F_i = 0 \quad \text{for } i = 1, 2, \dots, (j - 1), \tag{8a}$$

$$F_i = F_y + (F_u - F_y)(w_i/w_{cr})^\gamma \quad \text{for } i = j, \dots, (m - 1), \tag{8b}$$

$$w_i = 0 \quad \text{for } i = m, \dots, p, \tag{8c}$$

$$F_i = -[F_y + (F_u - F_y)(w_i/w_{cr})^\gamma] \quad \text{for } i = (p + 1), \dots, n. \tag{8d}$$

The same hardening law is used for tension, Eq. (8b), and compression, Eq. (8d). Eqs. (7) and (8) constitute an algebraic system of $(2n)$ equations with $(2n + 1)$ unknowns, i.e., the elements of the vectors $\{w\}$ and $\{F\}$ and the applied load, P . In this case, there are two alternative possible additional equations to solve the system: we can set either the force in the fictitious crack tip, m , equal to the tensile yielding force, or the force in the fictitious overlapping zone tip, p , equal to the compressive

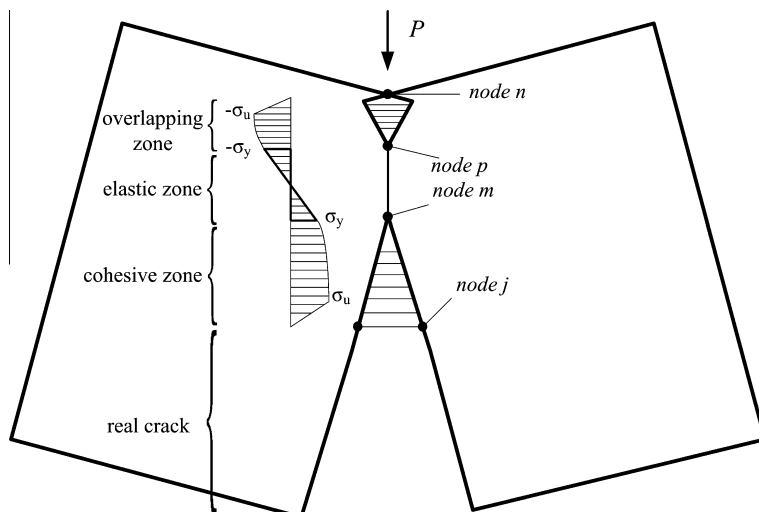


Fig. 7. Nonlinear cohesive and overlapping stress distributions along the mid-span cross-section of the TPB specimen.

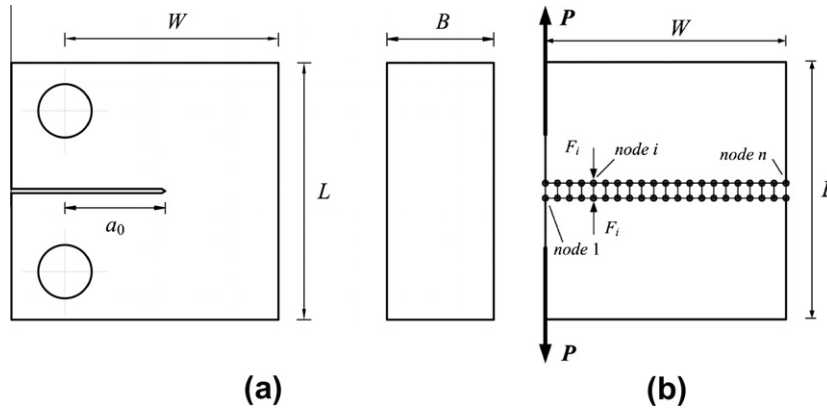


Fig. 8. Compact tension test: (a) geometry; and, (b) finite element nodes along the symmetry cross-section.

yielding force. In the numerical scheme, we select the situation which is closer to the critical condition. The driving parameter of the process is the position of the tip that in the considered step has reached the limit resistance. Only this tip is moved when passing to the next step. The two fictitious tips advance until they converge to the same node. Finally, at each step of the algorithm it is possible to calculate the deflection, δ , as follows:

$$\delta = \{D_w\}\{w\} + D_p P, \tag{9}$$

where $\{D_w\}$ is the vector of the coefficients of influence for the nodal displacements, and D_p is the coefficient of influence for the applied load. In addition, $\{D_w\}$ and D_p are also independent of the specimen size, mesh and beam slenderness being kept constant.

It is worth noting that the same numerical algorithm can be profitably used to study different specimen geometries and loading conditions, as, for instance, the compact tension test (CT). The only difference regards the elastic coefficients entering Eqs. (7) and (9). The geometry and the discretized model used to compute the elastic coefficients are shown in Fig. 8.

4. Limit analysis according to the hardening cohesive/overlapping zone model

4.1. Limit analysis for the three-point-bending test

The numerical simulation procedure carried out with the algorithm proposed in the previous section terminates when the two fictitious tips converge to the same node. On the other hand, for an exhaustive analysis, the entire post-peak load vs. deflection curve should be determined. To this purpose, a limit analysis approach based on the proposed constitutive laws can provide asymptotic approximation to the post-peak response, which can be relevant in the analysis of ductile-to-brittle transitions.

Once the tensile yielding strength and the compressive yielding strength have been achieved at the bottom and the top beam edges, respectively, fracture and plastic compressive processes are assumed to initiate. The supposed limit situation is shown in Fig. 9a. The limit stage of the deformation and fracture process may be considered as that of two rigid parts connected by the hinge A in the mid-span cross-section. The equilibrium of each part is ensured by the external load, the support reaction, the closing cohesive forces and the opening overlapping forces, as evidenced in Fig. 9b. For the sake of simplicity, a linear-hardening with subsequent vertical drop relationship is assumed for the stress vs. displacement law (dashed curve in Fig. 4c) instead of the power-law hardening expressed in Eq. (6) followed by the linear softening branch (solid curve in Fig. 4c). Several investigations focusing on the effect of the shape of the traction–separation law on the resulting fracture behavior (see, among others, Tvergaard and Hutchinson [33,34] for metals and Carpinteri et al. [44] for concrete-like materials), in fact, came to the conclusion that such an effect is relatively weak. On the contrary, as discussed in Section 6.1 of the present paper, the cohesive/overlapping dissipated energy plays a fundamental role in determining the overall response. Therefore, a simplified law can be assumed for the limit analysis computations, provided that the area beneath the stress vs. displacement curve is equal to that of the more complex law assumed for the corresponding numerical simulations. The same mechanical parameters (cohesive/overlapping energy, yielding stress, ultimate stress) are adopted for both tension and compression. The geometrical similitude of the triangles ABC and A'B'C' in Fig. 9a provides:

$$\frac{\delta}{0.5L} = \frac{0.5w_{cr}}{h}, \tag{10}$$

which gives:

$$h = \frac{w_{cr}L}{4\delta}. \tag{11}$$

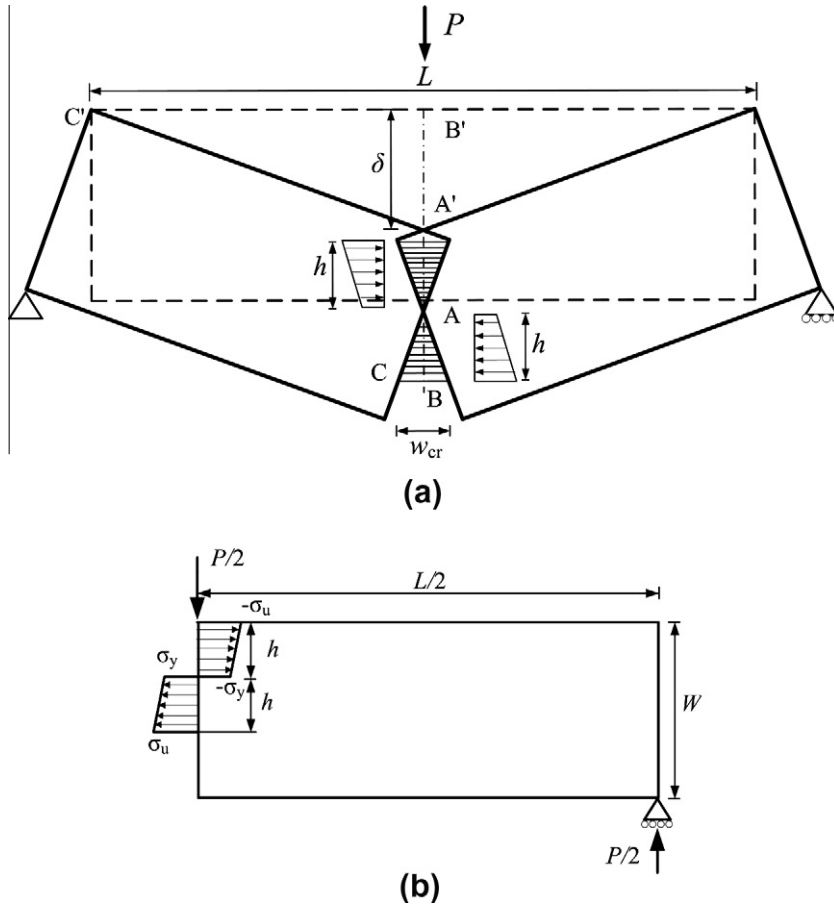


Fig. 9. Limit analysis for TPB test: (a) limit condition of fracture with cohesive and overlapping forces; (b) cohesive and overlapping force distributions along the symmetry cross-section.

The rotational equilibrium around point A is possible for any beam configuration only if the moment of external force and support reaction is equal to the moment of cohesive forces and overlapping forces (see Fig. 9b):

$$\frac{PL}{4} = \frac{1}{3} h^2 B (2\sigma_u + \sigma_y), \tag{12}$$

which gives

$$P = \frac{1}{12} w_{cr}^2 L B (2\sigma_u + \sigma_y) \delta^{-2}. \tag{13}$$

In dimensionless form, we have:

$$\tilde{P} = \frac{\lambda^4}{3} \left(\frac{2\sigma_u + \sigma_y}{\sigma_y} \right) \left(\frac{s_E}{\varepsilon_y \delta} \right)^2, \tag{14}$$

where

$$\tilde{P} = \frac{PL}{\sigma_y B W^2}, \tag{15}$$

$$\tilde{\delta} = \frac{\delta L}{\varepsilon_y W^2}, \tag{16}$$

and \$s_E\$ is the brittleness number defined in Eq. (5). According to Fig. 9a, the total extension of the cohesive and overlapping zones must be less than or equal to the initial ligament of the beam, so that the limit condition is:

$$2h \leq W(1 - \xi_0), \tag{17}$$

where ξ_0 is the ratio between the initial crack length, a_0 , and the beam depth, W . From Eqs. (11) and (17), we can obtain the lower bound to limit analysis in terms of deflection:

$$\delta \geq \frac{2w_{cr}}{(1 - \xi_0)}. \tag{18}$$

4.2. Limit analysis for the compact tension test

Once the yielding tensile or compressive strength has been achieved at one of the two ends of the initial ligament (point F or N in Fig. 10), the tensile cohesive process or the compressive overlapping process are supposed to initiate. Based on the hypothesis that the CT specimen is constituted by two rigid blocks connected by the plastic hinge A, as shown in Fig. 10, geometrical similitude and equilibrium conditions analogous to those previously considered in the limit analysis of TPB can be assumed. Again, a linear-hardening with subsequent vertical drop relationship is assumed for the stress vs. displacement law (see Fig. 4c).

In Fig. 10, M or M' is the point of load application, and α is the rotational angle around hinge A corresponding to the external load, P, which is equilibrated by the cohesive and overlapping forces exerted perpendicularly to the symmetry plane. W is the width of the CT specimen; h_1 and h_2 are the extensions of the cohesive and overlapping zones, respectively; w_{cr} is the critical opening or overlapping displacement; ξ_0 is the initial crack ratio, and B is the thickness of the specimen. As schematically shown in Fig. 10, C'F' is the initial crack length, a_0 . From the triangles M'AC' and FAF' in Fig. 10, being $FF' = w_{cr}/2$, $AF' = h_1$, $MC = M'C' = l_{MC} = l_{M'C'}$ and $AC' = W - h_2$, we have:

$$\tan \alpha = \frac{w_{cr}}{2h_1}, \tag{19}$$

and

$$\tan \beta = \frac{l_{MC}}{W - h_2}. \tag{20}$$

From triangles MAD and M'AC':

$$l_{MD} = l_{AM} \sin(\alpha + \beta), \tag{21}$$

$$l_{AM} = l_{AM'} = \left[l_{M'C'}^2 + (W - h_2)^2 \right]^{\frac{1}{2}}. \tag{22}$$

From Fig. 10, the load-line displacement, δ , is equal to:

$$\delta = 2(l_{MD} - l_{M'C'}) \tag{23}$$

Meanwhile, the moment equilibrium around hinge A can provide:

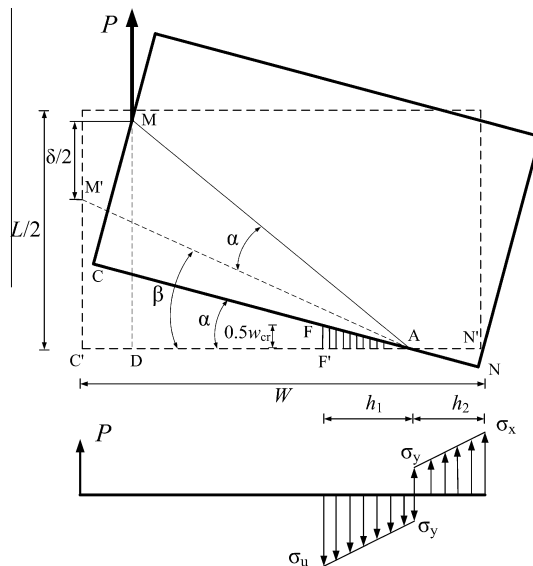


Fig. 10. Limit condition of fracture with cohesive and overlapping forces and geometrical similitude in the CT specimen.

$$P(W - h_2) = \frac{B}{6} \left[h_1^2 (2\sigma_u + \sigma_y) + h_2^2 (2\sigma_x + \sigma_y) \right], \quad (24)$$

and the force equilibrium perpendicular to the symmetry section gives:

$$P = 0.5B[(\sigma_u + \sigma_y)h_1 - (\sigma_x + \sigma_y)h_2], \quad (25)$$

where

$$\sigma_x = \frac{h_2}{h_1}(\sigma_u - \sigma_y) + \sigma_y \quad (26)$$

is the overlapping force at the end of the overlapping zone. As shown in Fig. 10, the total extension of the cohesive and overlapping zones must be less than or equal to the initial ligament of the CT specimen:

$$h_1 + h_2 \leq (1 - \xi_0)W. \quad (27)$$

Such a limitation determines a lower bound to the load-line displacement, beyond which the limit analysis assumes validity for the considered specimen with a given initial crack ratio ξ_0 .

5. Scale-independent (fractal) hardening cohesive/overlapping law

Although the cohesive approach is a significant contribution in the definition of a scale-independent constitutive law with respect to the classical stress–strain relations, the cohesive parameters, σ_y , w_{cr} and \mathcal{G}_F , are affected themselves by the specimen size. Therefore, the fractal approach to scale effects proposed and discussed widely by Carpinteri [25,26] and Carpinteri et al. [29,42] for quasi-brittle materials both in tension and compression, is herein adopted. As experimentally evidenced by Kleiser and Bocek [45] and Zaiser et al. [46] for copper alloy, in fact, the strain at the ultimate condition is localized within slip-line bands having fractal patterns. Analogously, the fractal geometry can be successfully used to represent the ligament at the peak load, characterized by the presence of voids and microcracks. Finally, transmission electron micrograph technique (TEM) [47] and acoustic emission technique [48] have confirmed the fractal character of the energy dissipation pattern. As a result, the nominal parameters of the cohesive law, namely σ_y , w_{cr} and \mathcal{G}_F , cannot be assumed as material properties, as they depend on the resolution used to measure the set where stress, strain and energy dissipation take place. In particular, in the limit of a very high measure resolution, the stress and the strain tend to be infinite, whereas the dissipated energy tends to zero. Finite values can be obtained only introducing fractal quantities, i.e., mechanical quantities with non-integer physical dimensions. On the other hand, if the measure resolution is fixed, the nominal quantities undergo size effects. More specifically, the fractal strain localization explains the observed increasing tail of the cohesive law as the specimen size increases, i.e., it clarifies the scaling of the critical displacement w_{cr} . The lacunarity of the ligament explains the experimentally observed decrease in the cohesive yielding strength, σ_y , by increasing the specimen size, whereas the scaling of the fracture energy is a consequence of the invasive fractality of the domain where energy dissipates, which has a physical dimension comprised between 2.0 and 3.0. In formulae, the scaling of the parameters is described by the following power-laws:

$$\sigma_y = \sigma_y^* W^{-d_\sigma}, \quad (28a)$$

$$\mathcal{G}_F = \mathcal{G}_F^* W^{d_G}, \quad (28b)$$

$$w_{cr} = \varepsilon_{cr}^* W^{(1-d_\varepsilon)}, \quad (28c)$$

where σ_y^* , \mathcal{G}_F^* and ε_{cr}^* are the true scale invariant parameters, having anomalous physical dimensions, and w is the representative specimen dimension. From a practical point of view, the exponents d_σ and d_G can be evaluated from experimental results. In particular, they represent the slope, in the bi-logarithmic diagram, of the straight lines interpolating the values of σ_y and \mathcal{G}_F , respectively, as functions of the specimen size. This means that, tensile and/or compressive tests have to be carried out on samples with different dimensions. Then, the exponent d_ε is obtained by applying the following relationship derived from the integral definition of the fractal fracture energy (see [29] for more details):

$$d_\sigma + d_\varepsilon + d_G = 1. \quad (29)$$

According to the fractal concepts herein outlined, it is possible to define a scale-independent hardening cohesive/overlapping law, which can be expressed in the following form:

$$\sigma^* = \sigma_y^* + (\sigma_u^* - \sigma_y^*)(\varepsilon^*/\varepsilon_y^*)^\gamma, \quad (30)$$

where the fractal parameters σ_y^* , σ_u^* , ε_y^* , as well as \mathcal{G}_F^* , are determined as the intercepts of the scaling-laws in Eq. (28).

6. Comparison between experimental results and numerical simulations

6.1. Three-point-bending test of HY80 steel

In this section, the experimental load vs. displacement curves from Zhu and Joyce [49] are compared with our numerical simulations. The material used for tests was HY80 steel available in a 27 mm thick plate with $\sigma_y = 630$ MPa, $\sigma_u = 735$ MPa, hardening exponent 0.1, and the Young's modulus $E = 207$ GPa, which are from the cylindrical specimen tensile test with a 25 mm initial gauge. The specimens were single edge notched as recommended by ASTM E1820, with different initial crack length ratios $\xi_0 = a_0/W = 0.13, 0.25, 0.40, 0.55, 0.60$. The other geometric parameters of the beams are: $L = 203$ mm, $W = 50.75$ mm, $B = 25.375$ mm, slenderness $\lambda = 4$.

The above mechanical parameters have been employed in the numerical simulations with the cohesive/overlapping laws. The cohesive/overlapping energy is assumed to be 750 N/mm, $w_{cr} = 1.81$ mm and $w_r = 0.3w_{cr}$. It is worth noting that the ratio w_r/w_{cr} has only a slight influence on the pre-peak behavior but not trivial beyond that, as can be deduced from the load vs. deflection curves shown in Fig. 11b. Such curves refer to the three different constitutive laws characterized by $w_r/w_{cr} = 0.1, 0.5$ and 0.9 , shown in Fig. 11a. On the contrary, the mechanical response, especially the post-peak performance, is significantly determined by the value of the cohesive energy (see Fig. 12).

It is worth noting that the assumed value, $G_F = 750$ N/mm, is approximately equal to the asymptotic value J_{ss} of the J -resistance curves in [49]. The comparison between experiments and numerical simulations is shown in Fig. 13, where a very good approximation is obtained for all the considered initial crack lengths. The numerical simulations are terminated when the two fictitious tips converge to the same node, so that the tails of the load vs. deflection curves are described just by means of limit analysis. In addition, the numerical load–deflection curve for $a_0/W = 0.00$ is also plotted in Fig. 13, which demonstrates a very good continuity between numerical algorithm and limit analysis. The points A, B, C, D, E and F indicate the lower bounds of limit analysis for the different initial crack ratios, $\xi_0 = a_0/W$. It may be presumed that all the experimental load–deflection curves asymptotically tend to the limit analysis curve as shown in Fig. 13.

6.2. Compact tension test of DIN 22NiMoCr37 steel

The material for the compact tension test (CT) was obtained from a large forged, quenched and tempered ring segment of ferritic steel DIN 22NiMoCr37, which is widely used in nuclear power plants. All the experimental data are taken from the Euro-Fracture Dataset [50]. Three different specimens scaled in linear dimension as 1:2:4 have been considered, as described in Table 1. According to the scale effects discussed in Section 5, size-dependent parameters should be assumed for the constitutive laws. Unfortunately, the tensile properties were determined only from cylindrical specimens having a diameter of 6 mm and an initial gauge length of 25 mm. They are: $\sigma_y = 470$ MPa, $\sigma_u = 616$ MPa, and $E = 200$ GPa. Therefore, the scale-dependent cohesive parameters for the numerical and analytical simulations cannot be obtained from experiments, but they have to be derived from a best-fitting analysis. In particular, the properties reported in ref. [50] are assigned to the 1T CT specimen, which has the dimensions closest to those of the tensile sample. For such a specimen, the cohesive/overlapping energy is assumed equal to 3200 N/mm, and the Ramberg–Osgood hardening exponent to 0.12. Then, a variation of the yielding strength with a slope of -0.15 in the bi-logarithmic diagram σ_y vs. W , is introduced, consistently with the experimental investigations on the size effects in the bending test of mild steel reported in [51]. Such a scaling law (Eq. (28a)) determines $\sigma_y = 425$ and 385 MPa for 2T and 4T CT specimens, respectively (see Fig. 14a). As regards the scale effect on the cohesive/overlapping energy, it is determined by repeated solutions until the numerical and limit analysis predictions best fit the

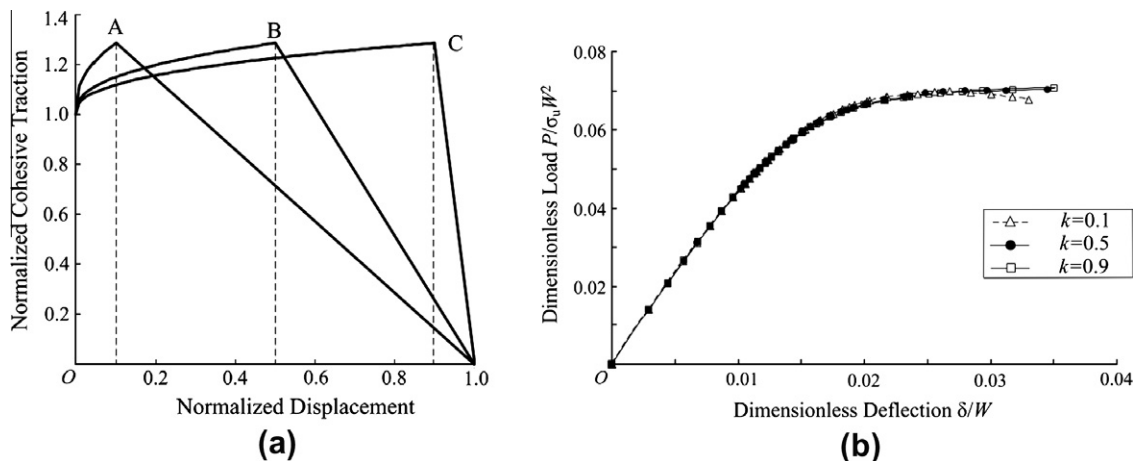


Fig. 11. Normalized cohesive/overlapping laws by varying $k = w_r/w_{cr}$ (a); and corresponding dimensionless load vs. deflection curves (b).

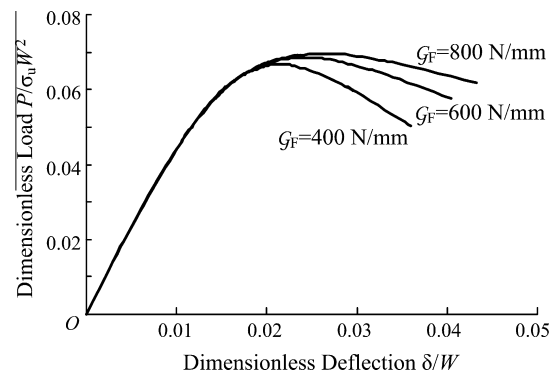


Fig. 12. Dimensionless load vs. deflection curves for different cohesive/overlapping energy G_F .

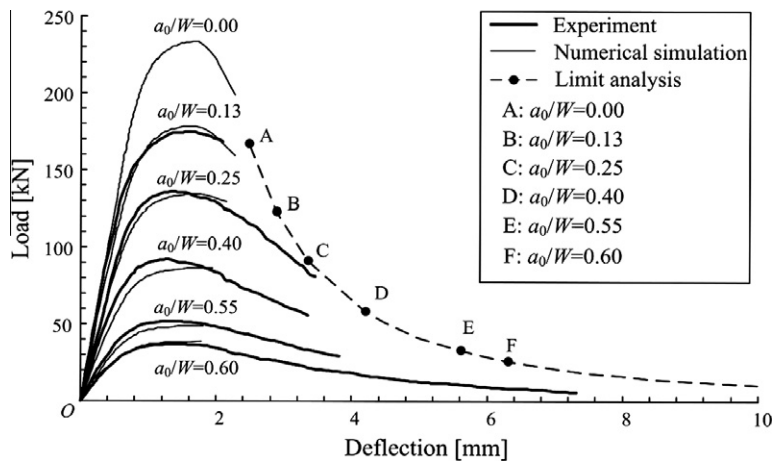


Fig. 13. Comparison of numerical simulations with experimental results [49] for the TPB tests with different initial crack lengths (the points A, B, C, D, E, F represent the lower bound of limit analysis for different initial crack lengths).

Table 1

Geometry of the CT specimens of DIN 22NiMoCr37 steel [50].

Specimen	Width, W (mm)	Thickness, B (mm)	Initial crack length, a_0 (mm)
CT 1T	50	25	28.3
CT 2T	100	50	58.9
CT 4T	200	100	113.6

experimental results (Fig. 15). Also in these cases, the numerical simulations are terminated when the two fictitious tips converge to the same node, and the asymptotic tails of the load vs. deflection curves are obtained from the limit analysis approach. The resulting power-law exponent, d_G , is 0.50, according to which the values $G_F = 4100$ and 6400 N/mm correspond to specimens 2T and 4T CT, respectively (Fig. 14b). The parameter w_{cr} is determined from σ_y and G_F once the shape of the cohesive law and the ratio w_r/w_{cr} are fixed. From the size-dependent cohesive laws used for the simulations, and shown in Fig. 16a, the corresponding fractal cohesive laws can be derived by applying the inverse of Eq. (28) (see Fig. 16b). Such curves are coincident in the hardening portion, confirming the validity of the fractal approach in determining size-independent constitutive laws. The average values for the fractal parameters are: $\sigma_y^* = 848.50$ N/mm^{1.85}, $\sigma_u^* = 1112.00$ N/mm^{1.85}, $\epsilon_y^* = 0.48$ mm/mm^{0.65}, and $G_F^* = 438.00$ N/mm^{1.50}.

6.3. Compact tension test of JLF-1LN steel

The selected material was the JLF-1LN steel, and the fracture tests were carried out according to the ASTM E1820-99a [52]. Here the tensile properties were obtained from cylindrical specimens with a diameter of 6.25 mm and an initial gauge length of 40 mm. The yield strength is 450 MPa, the ultimate tensile strength is 620 MPa. Two specimens with dimensions scaled as 1:2 were considered (see Table 2).

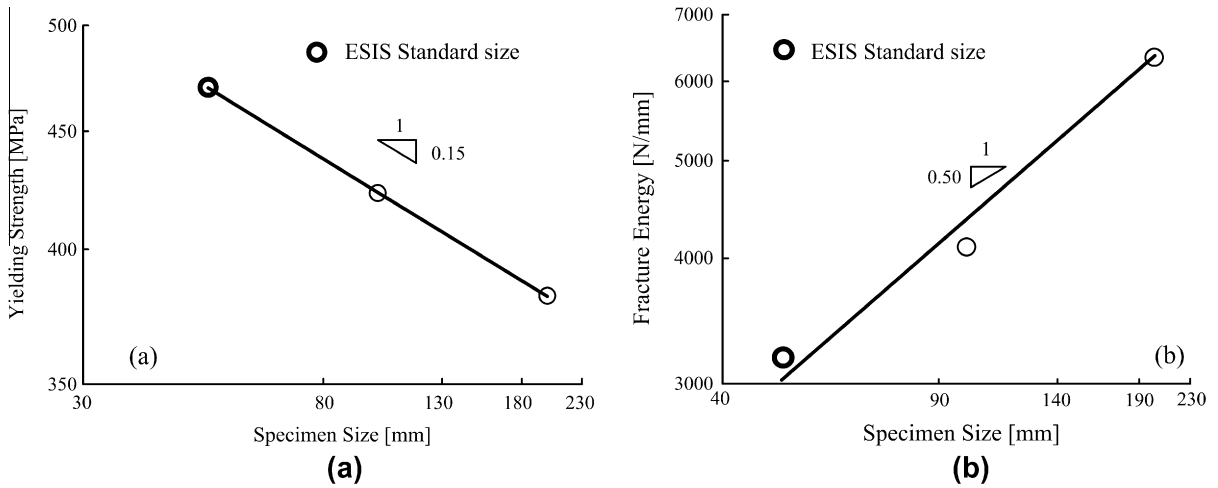


Fig. 14. Yielding strength (a) and cohesive/overlapping energy (b) vs. specimen size, in bi-logarithmic diagrams.

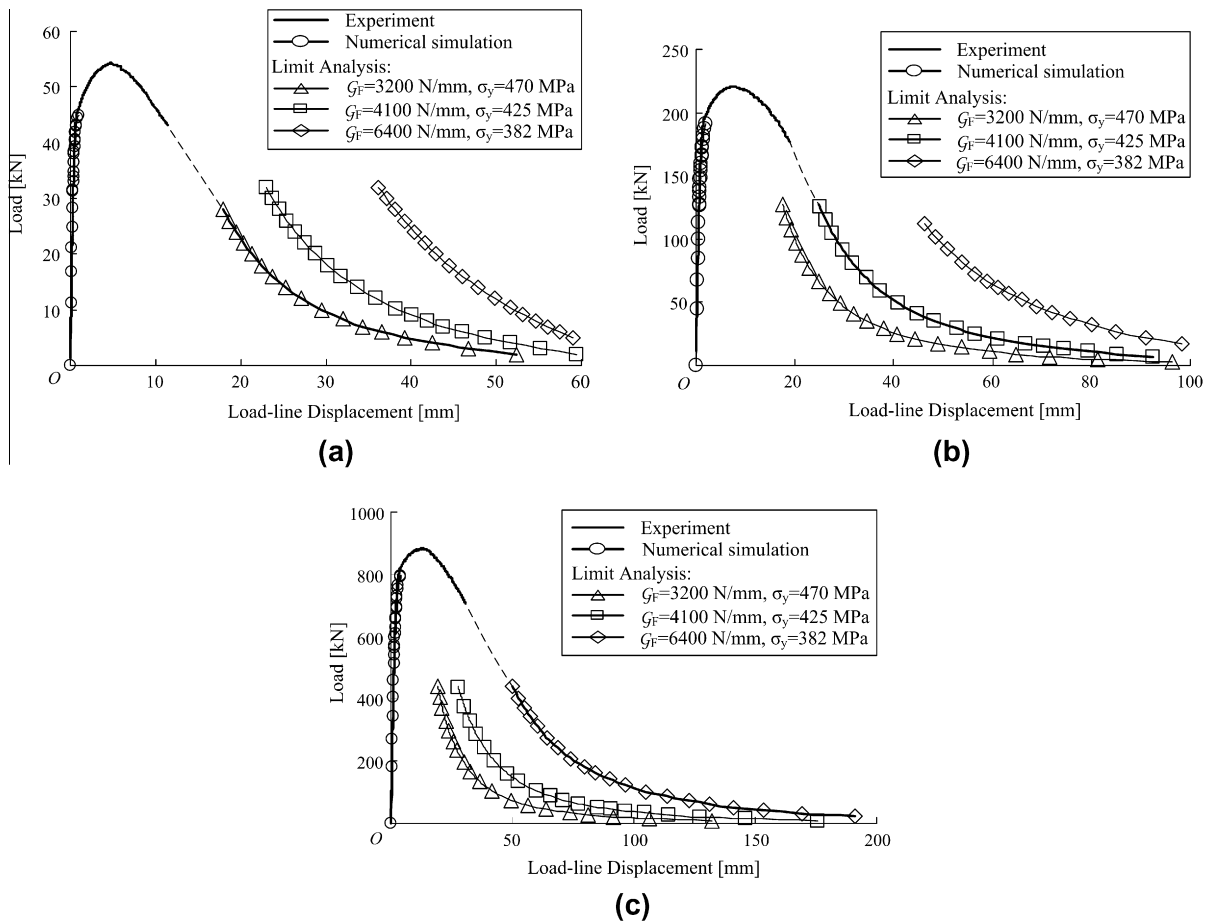


Fig. 15. Comparison between experimental results [50], numerical simulations and limit analysis predictions for 1T, 2T and 4T CT specimens.

A symmetric cohesive/overlapping law is used in the numerical simulations. The cohesive/overlapping parameters $\sigma_y = 450$ MPa, $\sigma_u = 620$ MPa and $G_F = 1600$ N/mm, to which corresponds $w_{cr} = 2.04$ mm, are assigned for 1T CT specimen. Then, analogously to the previous section, a scaling law with slope -0.15 is assumed for the yielding strength, determining $\sigma_y = 500$ MPa for specimen 1/2T (see Fig. 17a). A good continuity between experiments and limit analysis results is obtained

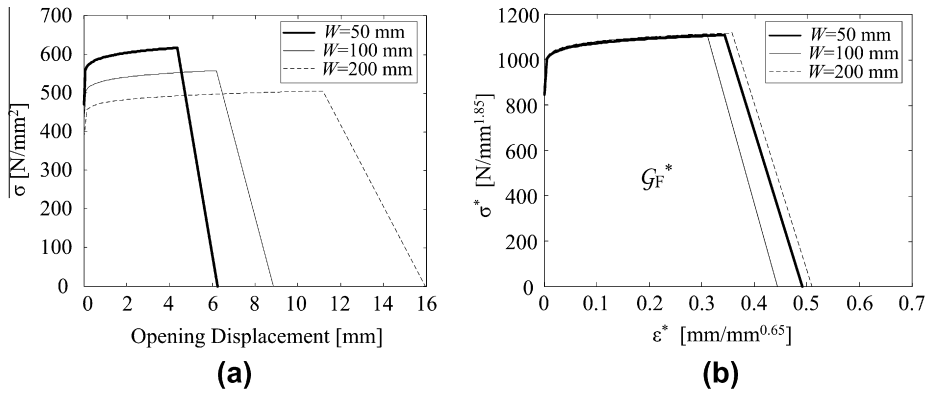


Fig. 16. Hardening cohesive laws for different specimen sizes (a); fractal hardening cohesive laws σ^* vs. ϵ^* (b).

Table 2

Geometry of the CT specimens of JLF-1LN steel [52].

Specimen	Width, W (mm)	Thickness, B (mm)	Initial crack length, a_0 (mm)
CT 1/2T	25.4	12.7	14.8
CT 1T	50.8	24.0	32.1

if the cohesive/overlapping energies 1100 and 1600 N/mm are assumed for the CT specimens 1/2T and 1T, respectively (Fig. 18). Again, the cohesive/overlapping energy varies linearly with the extreme slope 0.50 in the bi-logarithmic diagram, according to the fractal interpretation (see Fig. 17b).

7. Ductile-to-brittle transition

Dimensionless load–deflection diagrams for metallic beams subjected to TPB test are numerically obtained and plotted in Fig. 19, for $L = 4W$ and $16W$, different values of the energy brittleness number s_E , and a ratio σ_u/σ_y equal to 1.17. The initial crack depth, a_0/W , is constant and equal to 0.25.

A transition from ductile to brittle response occurs by decreasing the energy brittleness number and/or increasing the specimen slenderness. In particular, it has to be emphasized that a snap-back branch appears for low cohesive/overlapping energy, high tensile strength, large specimen size and slenderness (see Fig. 19), even if a very ductile constitutive law with extended hardening branch is assumed. The $P-\delta$ curves tend to present steeper negative or even positive slope in the post-peak branch leading to catastrophic events if the loading process is deflection-controlled. Such indenting branch is not virtual only if the loading process is controlled by a monotonically increasing function of time, such as the crack and

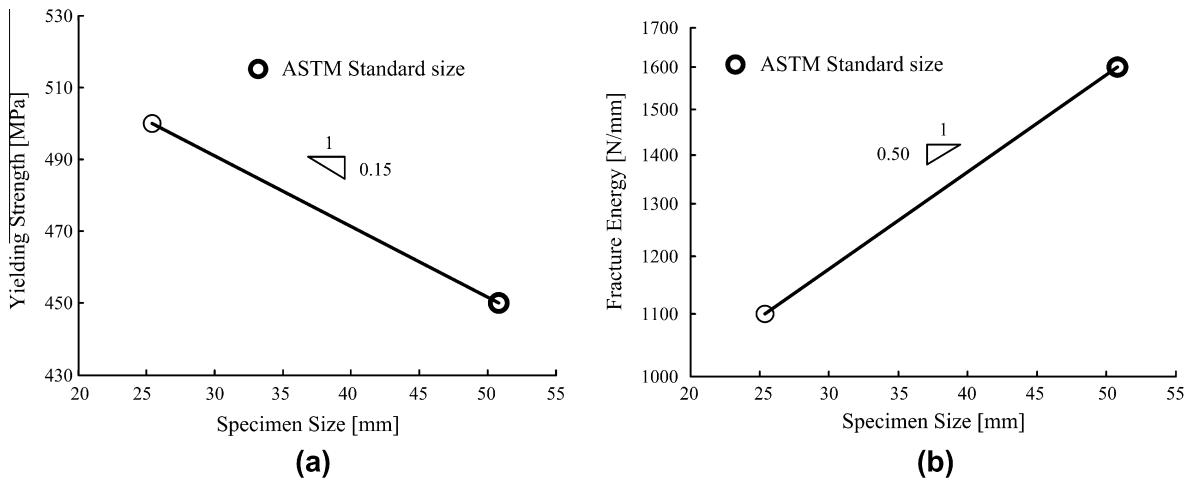


Fig. 17. Yielding strength (a) and cohesive/overlapping energy (b) vs. specimen size, in bi-logarithmic diagrams.

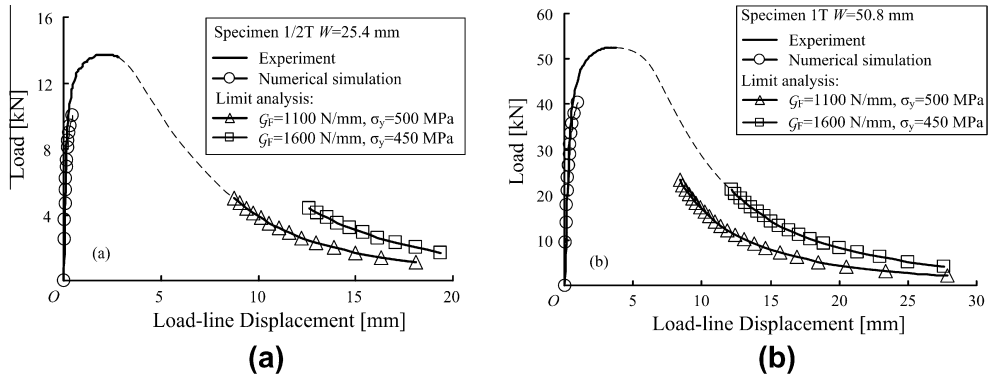


Fig. 18. Comparison between experimental results [52], numerical simulations and limit analysis predictions for 1/2T and 1T CT specimens.

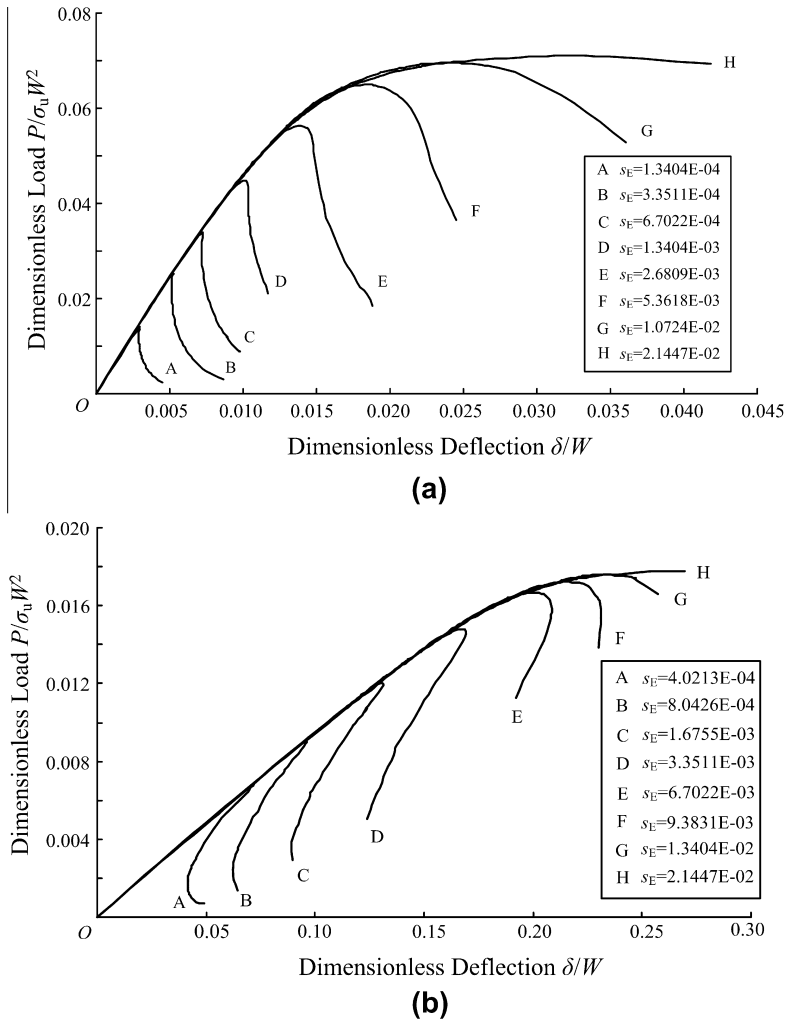


Fig. 19. Dimensionless load vs. deflection diagrams (TPBs) for the beam slenderness $\lambda = 4$ (a) and 16 (b) by varying the brittleness number s_E .

overlapping extensions, or the crack mouth opening displacement. When the post-peak behavior is kept under control up to the complete specimen separation, the area beneath the load–deflection curve represents the product of cohesive/overlapping energy by the initial cross-section ligament area. The areas under the $P-\delta$ curves are thus proportional to the respective s_E numbers. This simple result is due to the assumption that energy dissipation occurs only on the fracture surface numbers.

8. Discussion and conclusions

It is widely accepted that J -integral, R -resistance curve and even K_{IC} can be applied as crack initiation criteria for metallic materials, and those approaches indeed enjoy a great success in some sense. However, as regards the crack propagation phase or the post-peak behavior, their predictions are far insufficient, although these aspects are crucial in structural integrity assessment. In addition, those classical fracture parameters usually appear as size-dependent.

In this paper, a hardening cohesive/overlapping zone model is proposed for the analysis of complex mechanical phenomena in fracture of metallic materials. The plastic dissipation in the bulk and the crack formation and propagation are taken into account by assuming a hardening cohesive/overlapping constitutive law, whereas a linear elastic behavior is considered beyond the process zone. Subsequently, the numerical algorithm [41] is developed with the hardening cohesive/overlapping constitutive law for both the TPB test and the CT test. A limit analysis using the same proposed constitutive model is adopted to capture the post-peak branches of the load vs. deflection curve. The comparison between experiments, numerical simulations, and limit analysis confirm the capacity of the approach to describe the effects of the size-scale and of the initial crack length. Finally, the present model is used to obtain a transition from ductile to brittle response by decreasing the energy brittleness number and/or increasing the specimen slenderness. In particular, a snap-back branch appears for low cohesive/overlapping energy, high tensile strength and large specimen size, even if a very ductile constitutive law with extended hardening branch is assumed. It is demonstrated how the energy brittleness number s_E could be a characteristic parameter to evaluate the fracture instability not only in quasi-brittle materials [15,53] but also in metallic materials under certain conditions. Future developments of the present research will regard experimental investigations over a broad scale range of single edge notched beams subjected to TPB test, in order to further validate the proposed model.

Acknowledgments

The financial supports provided by the Ministry of University and Scientific Research (MIUR) to the project “Advanced applications of Fracture Mechanics for the study of integrity and durability of materials and structures”, and by the China Scholarship Council (CSC) are gratefully acknowledged.

References

- [1] Rice JR. A path independent integral and the approximate analysis of strain concentration by notches and cracks. *J Appl Mech* 1968;15:379–86.
- [2] Anderson TL. *Fracture mechanics: fundamentals and applications*. 2nd ed. Boca Raton: CRC Press; 1995.
- [3] Turner CE, Kolednik OA. A micro and macro approach to the energy dissipation rate model of stable ductile crack growth. *Fatigue Fract Engng Mater Struct* 1994;17:1089–107.
- [4] Sumpter JDG. The energy dissipation rate approach to tearing instability. *Engng Fract Mech* 2004;71:17–37.
- [5] Barenblatt GI. The formation of equilibrium cracks during brittle fracture: general ideas and hypotheses. *J Appl Math Mech* 1959;23:622–36.
- [6] Barenblatt GI. The mathematical theory of equilibrium cracks in brittle fracture. *Adv Appl Mech* 1962;7:55–129.
- [7] Dugdale DS. Yielding of steel sheets containing slits. *J Mech Phys Solids* 1960;8:100–14.
- [8] Bilby BA, Cottrell AH, Swinden KH. The spread of plastic yield from a notch. *Proc Roy Soc London A* 1963;272:304–14.
- [9] Willis JR. A comparison of the fracture criteria of Griffith and Barenblatt. *J Mech Phys Solids* 1967;15:151–62.
- [10] Wnuk MP. Quasistatic extension of a tensile crack contained in viscoelastic–plastic solid. *J Appl Mech* 1974;41:234–42.
- [11] Hillerborg A, Modeer M, Petersson PE. Analysis of crack formation and crack growth in concrete by means of fracture mechanics and finite elements. *Cem Concr Res* 1976;6:773–82.
- [12] Wecharatana M, Shah SP. Prediction of non-linear fracture process zone in concrete. *J Engng Mech (ASCE)* 1983;109:1231–46.
- [13] Bažant ZP, Oh BH. *Concrete fracture via stress–strain relations*. Technical report 81-10/665c, center for concrete and geomaterials, Northwestern University, 1981.
- [14] Ingraffea AR, Gerstle WH. Nonlinear fracture models for discrete crack propagation. In: Shah SP, editor. *NATO: advanced research workshop on application of fracture mechanics to cementitious composites*. Dordrecht: Martinus Nijhoff; 1984. p. 171–209.
- [15] Carpinteri A. Interpretation of the Griffith instability as a bifurcation of the global equilibrium. In: Shah SP, editor. *Application of fracture mechanics to cementitious composites*. The Netherlands: Martinus Nijhoff; 1985. p. 284–316.
- [16] Carpinteri A. Cusp catastrophe interpretation of fracture instability. *J Mech Phys Solids* 1989;37:567–82.
- [17] Carpinteri A. Decrease of apparent tensile and bending strength with specimen size: two different explanations based on fracture mechanics. *Int J Solids Struct* 1989;25:407–29.
- [18] Carpinteri A. Size effects on strength, toughness and ductility. *J Engng Mech (ASCE)* 1989;115:1375–92.
- [19] Carpinteri A, Di Tommaso A, Fanelli M. Influence of material parameters and geometry on cohesive crack propagation. In: Wittmann FH, editor. *Fracture toughness and fracture energy of concrete (proceedings of an international conference on fracture mechanics of concrete, Lausanne, Switzerland, 1985)*. Amsterdam: Elsevier Science Publisher; 1986. p. 117–35.
- [20] Carpinteri A, Colombo G, Giuseppetti G. Accuracy of the numerical description of cohesive crack propagation. In: Wittmann FH, editor. *Fracture toughness and fracture energy of concrete (proceedings of an international conference on fracture mechanics of concrete, Lausanne, Switzerland, 1985)*. Amsterdam: Elsevier Science Publisher; 1986. p. 189–95.
- [21] Carpinteri A, Di Tommaso A, Ferrara G, Melchiorri G. Experimental evaluation of concrete fracture energy through a new identification method. In: Wittmann FH, editor. *Fracture toughness and fracture energy of concrete (proceedings of an international conference on fracture mechanics of concrete, Lausanne, Switzerland, 1985)*. Amsterdam: Elsevier Science Publisher; 1986. p. 423–36.
- [22] Carpinteri A, Valente S. Numerical modelling of mixed-mode cohesive crack propagation. In: Atluri SN, Yagawa G, editors. *Computational mechanics '88 (proceedings of the international conference on computational engineering science, Atlanta, USA, 1988)*, vol. 1. Berlin: Springer-Verlag; 1988 [12–VI].
- [23] Cen Z, Maier G. Bifurcations and instabilities in fracture of cohesive-softening structures: a boundary elements analysis. *Fatigue Fract Engng Mater Struct* 1992;15:911–28.
- [24] Elices M, Guinea GV, Planas J. Prediction of size-effect based on cohesive crack model. In: Carpinteri A, editor. *Size-scale effects in the failure mechanisms of materials and structures*. E&FN Spon; 1996. p. 309–24.
- [25] Carpinteri A. Fractal nature of material microstructure and size effects on apparent mechanical properties. *Mech Mater* 1994;18:89–101.

- [26] Carpinteri A. Scaling laws and renormalization groups for strength and toughness of disordered materials. *Int J Solids Struct* 1994;31:291–302.
- [27] Carpinteri A, Chiaia B, Ferro G. Size effects on nominal tensile strength of concrete structures: multifractality of material ligaments and dimensional transition from order to disorder. *Mater Struct* 1995;28:311–7.
- [28] Carpinteri A, Chiaia B. Multifractal nature of concrete fracture surfaces and size effects on nominal fracture energy. *Mater Struct* 1995;28:435–43.
- [29] Carpinteri A, Chiaia B, Cornetti P. A scale-invariant cohesive crack model for quasi-brittle materials. *Engng Fract Mech* 2002;69:207–17.
- [30] Carpinteri A, Ferro G. Size effects on tensile fracture properties: a unified explanation based on disorder and fractality of concrete microstructure. *Mater Struct* 1994;28:563–71.
- [31] van Mier JGM, van Vliet MRA. Effect of strain gradients on the size effect of concrete in uniaxial tension. *Int J Fract* 1999;94:195–219.
- [32] Carpinteri A, Cornetti P, Puzzi S. Scaling laws and multiscale approach in the mechanics of heterogeneous and disordered materials. *Appl Mech Rev* 2008;59:283–305.
- [33] Tvergaard V, Hutchinson JW. The relation between crack growth resistance and fracture process parameters in elastic–plastic solids. *J Mech Phys Solids* 1992;40:1377–97.
- [34] Tvergaard V, Hutchinson JW. Effect of T-stress on mode I crack growth resistance in a ductile solid. *Int J Solids Struct* 1994;31:823–33.
- [35] Siegmund T, Brocks W. Prediction of the work of separation in ductile failure and implications to the modeling of ductile failure. *Int J Fract* 1999;99:97–116.
- [36] Gurson AL. Plastic flow and fracture behaviour of ductile materials incorporating void nucleation, growth and coalescence. PhD thesis, Brown University, 1975.
- [37] Tvergaard V, Needleman A. Analysis of the cup-cone fracture in a round tensile bar. *Acta Metall* 1984;32:57–169.
- [38] Zhang ZL, Thaulow C, Ødegård J. A complete Gurson model approach for ductile fracture. *Engng Fract Mech* 2000;67:155–68.
- [39] Siegmund T, Brocks W. A numerical study on the correlation between the work of separation and the dissipation rate in ductile fracture. *Engng Fract Mech* 2000;67:139–54.
- [40] Jin Z-H, Sun CT. Cohesive fracture model based on necking. *Int J Fract* 2005;134:91–108.
- [41] Carpinteri A, Corrado M, Paggi M, Mancini G. New model for the analysis of size-scale effects on the ductility of reinforced concrete elements in bending. *J Engng Mech (ASCE)* 2009;135:221–9.
- [42] Carpinteri A, Corrado M. An extended (fractal) overlapping crack model to describe crushing size-scale effects in compression. *Engng Failure Anal* 2009;16:2530–40.
- [43] Hull D, Bacon DJ. Introduction to dislocations. 4th ed. Butterworth-Heinemann; 2001.
- [44] Carpinteri A, Colombo G, Ferrara G, Giuseppetti G. Numerical simulation of concrete fracture through a bilinear softening stress-crack opening displacement law. In: Shah SP, Swartz SE, editors. Fracture of concrete and rock (proceedings of a SEM-RILEM international conference, Houston, USA, 1987). New York: Springer-Verlag; 1989. p. 131–41.
- [45] Kleiser T, Bocek M. The fractal nature of slip in crystals. *Z Metallkd* 1986;77:582–7.
- [46] Zaiser M, Bay K, Hähner P. Fractal analysis of deformation-induced dislocation patterns. *Acta Mater* 1999;47:2463–76.
- [47] Hähner P, Bay K, Zaiser M. Fractal dislocation patterning during plastic deformation. *Phys Rev Lett* 1998;81:2470–3.
- [48] Miguel MC, Vespignani A, Zapperi S, Weiss J, Grasso JR. Intermittent dislocation flow in viscoplastic deformation. *Nature* 2001;410:667–71.
- [49] Zhu X-K, Joyce JA. J-resistance curve testing of HY80 steel using SE(B) specimens and normalization method. *Engng Fract Mech* 2007;74:2263–81.
- [50] Heerens J, Hellmann D. Development of the Euro fracture toughness dataset. *Engng Fract Mech* 2002;69:421–49.
- [51] Richards CW. Size effect in the tension test of mild steel. *Proc Am Soc Test Mater* 1954;54:995–1000.
- [52] Ono H, Kasada R, Kimura A. Specimen size effects on fracture toughness of JLF-1 reduced-activation ferritic steel. *J Nucl Mater* 2004;329–33:1117–21.
- [53] Carpinteri A, editor. Nonlinear crack models for nonmetallic materials. Kluwer Academic Publishers; 1999.